Available online at www.sciencedirect.com
SCIENCE DIRECT®
Nuclear Instruments and Methods in Physics Research A 507 (2003) 643–656
NUCLEAR INSTRUMENTS & METHODS IN PHYSICS RESEARCH Section A
www.elsevier.com/locate/nima

SICANE: a detector array for the measurement of nuclear recoil quenching factors using a monoenergetic neutron beam

E. Simon[a], L. Bergé[b], A. Broniatowski[b], R. Bouvier[a], B. Chambon[a], M. De Jésus[a], D. Drain[a], L. Dumoulin[b], J. Gascon[a,*], J.-P. Hadjout[a], A. Juillard[b], O. Martineau[a], C. Pastor[a], M. Stern[a], L. Vagneron[a]

[a] *IPN Lyon, IN2P3-CNRS, Université Claude Bernard Lyon I, 4 rue Enrico Fermi, F-69622 Villeurbanne Cedex, France*
[b] *CSNSM, IN2P3-CNRS, Université Paris XI, Bât. 108, F-91405 Orsay Cedex, France*

Received 6 January 2003; received in revised form 20 March 2003; accepted 3 April 2003

Abstract

SICANE is a neutron scattering multidetector facility for the determination of the quenching factor (ratio of the response to nuclear recoils and to electrons) of cryogenic detectors used in direct WIMP searches. Well-collimated monoenergetic neutron beams are obtained with inverse (p, n) reactions. The facility is described, and results obtained for the quenching factors of scintillation in NaI(Tl) and of heat and ionization in Ge are presented.

PACS: 29.40.Wk; 29.40.Mc; 28.20.Cz; 95.35.+d

Keywords: Neutron scattering; Nuclear recoils; Quenching factor; NaI and Ge detectors; Bolometers; Dark matter

1. Introduction

Since 1985 [1], various experimental techniques have been proposed to detect the nuclear recoils that would be produced by the scattering of WIMP dark matter particles from our galactic halo (for a recent review of experimental searches, see e.g. Ref. [2]). The goal is to be sensitive to recoil energies down to 10 keV [3], at event rates well below one per kilogram of detector material per day [4]. For this, the detector response to low-energy nuclear recoils must be well known. Depending on the detection process (ionization, scintillation or heat), this response may differ significantly from that inferred from calibration with electron or γ-ray sources. A quantity of interest is thus the *quenching factor*, defined as the ratio of the signal amplitudes induced by a nuclear recoil and an electron of the same energy. This factor depends mainly on the detector material, the energy of the recoil and the detection process, although temperature and alignment effects may play a role (see e.g. Ref. [5]).

Quenching factor measurements have been made on scintillation detectors such as NaI [6], CsI [7], CaF_2 [8] and Xe [9], leading to values ranging from 4 to 30% depending on the recoil

*Corresponding author. Tel.: +33-472-431068.
E-mail address: gascon@ipnl.in2p3.fr (J. Gascon).

0168-9002/03/$ - see front matter
doi:10.1016/S0168-9002(03)01438-4

nucleus and its energy, and on the material in which the recoil takes place. The measured quenching factors of ionization detectors such as Si [10] or Ge [11–14] vary between 25 and 40% and appear to follow the recoil energy dependence predicted by the Lindhart theory [16]. More recently, the thermal detection efficiency for recoiling nuclei has been measured in a TeO_2 cryogenic detector, giving a thermal quenching factor slightly above unity [17].

The purpose of the SICANE facility (SIte de CAlibration NEutron) is the measurement of quenching factors of cryogenic detectors using nuclear recoils induced by monoenergetic neutron beams. The facility has been commissioned with tests using scintillation in an NaI(Tl) crystal and measurements of quenching factors for ionization and heat signals in a germanium cryogenic detector developed by the EDELWEISS collaboration.

2. Experimental procedure

2.1. Principle and motivation

The basic method for the measurement of the quenching factor of a detector is the following. First, the detector response to electron recoils is obtained using calibrated γ-ray source. This yields the calibration of the signal amplitude in terms of an *electron-equivalent* energy, E_{ee}. In a second step, the detector is exposed to a source producing nuclear recoils with a known kinetic energy E_R. The quenching factor Q is then

$$Q = \frac{E_{ee}}{E_R}. \quad (1)$$

The main difficulty for a precise and efficient measurement is the production of recoils with known E_R values.

In the present method, nuclear recoils are produced by neutron scattering. Other methods for producing nuclear recoils exist, such as the implantation of α-particle sources close to the surface of the detector [17,18]. When the α escapes the detector, the response of the detector to the recoiling daughter can be measured accurately. Alternatively, one can deduce the quenching for the daughter nucleus from the difference between the total energy deposited when the α decay occurs in the bulk and when it occurs near the surface with the daughter escaping detection [17]. However, this method is not adequate for ionization detectors, as their response may differ according to whether the interaction occurs close to surface or in the bulk of the volume [19]. Another drawback is that the recoiling daughter is often very different from the detector material. Neutron interactions have the advantage of occurring rather uniformly throughout the detector volume. The recoil nuclei thus produced are identical to those that would be induced by WIMP scattering.

In Ge cryogenic detectors with simultaneous read-out of the heat and ionization signals, the recoil energy can be measured event-by-event, independently of the nature of the recoil (electron or nuclear). In this type of detector, it is possible to directly measure the *ratio* of the ionization and heat quenching values[1] as a function of recoil energy [13]. If one assumes that the heat quenching factor Q' is unity,[2] these data can be interpreted as ionization quenching measurements. Alternatively, these data can be compared to the available direct measurements of ionization quenching in order to provide a verification of how close to unity are the heat quenching factors [13]. This comparison assumes that the ionization quenching factors do not depend on temperature, as all direct measurements [11,12,14] were performed at liquid nitrogen temperature (77 K) instead of cryogenic temperatures (~25 mK). The method based on the Q/Q' ratio cannot be applied to detectors with a single read-out, or to heat-and-scintillation detectors, as the amount of energy escaping as light is difficult to control. In addition, scintillation yields are known to depend on crystal temperature (see e.g. Ref. [15]).

[1] For clarity, from now on the symbol for ionization or scintillation quenching factors will be Q, and Q' will be used to represent heat quenching factors.

[2] This assumption is reasonable if the detector can be approximated as a close system where all the excitation energy is thermalized within a time scale inferior to that of the read-out of the heat signal and no energy is stored in crystal defects or other long-life processes.

Clearly, a method providing nuclear recoils of a known energy is relevant for the calibration of cryogenic detectors. In a non-relativistic elastic neutron scattering, the energy of the recoil nuclei E_R is given by

$$E_R(\theta) = E_n \frac{4Mm_n}{(m_n + M)^2} \frac{(1 - \cos\theta)}{2} \quad (2)$$

where E_n is the incident neutron kinetic energy, θ is the neutron scattering angle in the center-of-mass frame and m_n and M are the neutron and nucleus masses, respectively. Even with a monoenergetic neutron beam, E_R values vary from zero to $E_R(180^\circ)$. In experiments where θ is not measured, some information about the quenching factor can be obtained from the maximum E_{ee} value observed for a given E_n, the quenching factor being then equal to $E_{ee}/E_R(180^\circ)$ [11]. A more precise measurement consists in measuring the scattering angle of the neutron [11]. This requires neutron detectors with a small solid angle. However, in order to be efficient the total solid angle for the detection of the scattered neutrons must be as large as possible. This is a crucial point for performing in a reasonable time quenching factor measurements of cryogenic heat detectors, as their response is intrinsically slow.

These precision and efficiency constraints naturally lead to a concept of a large array of neutron detectors. With 48 neutron detectors, SICANE is the largest existing array. With such an extensive array, scattering at different angles can be measured simultaneously, reducing the systematic errors, and improving the diagnostic tools to identify the various background sources.

The basic performance of this array can readily be tested using scattering on a small NaI detector at room temperature, for which scintillation quenching data already exist [6]. For actual measurements on cryogenic detectors, two new potential problems arise. Firstly, the cryostat surrounding the detector represents an important amount of additional material where neutrons may scatter before or after interacting in the detector itself. Secondly, cryogenic detectors are intrinsically slow, and some care must be taken in establishing clean coincidences with the relatively faster array of neutron detectors while retaining a sufficiently high count rate. For the commissioning measurements of an actual cryogenic detector, a Ge heat-and-ionization detector was chosen as the experimental situation for these detectors is rather well controlled (see above), while still awaiting direct measurements of the low-temperature behavior of both Q and Q'.

2.2. Neutron beams

Up to now, experiments involving these techniques used monoenergetic neutrons produced by deuteron beam interactions on a deuterated target, or by a proton beam interacting on a ^{7}Li target [14]. The neutron emission in these reactions is almost isotropic. This reduces the flux impinging on the target detector, and imposes that the scattered-neutron detector array be very carefully shielded from direct neutrons [20], putting severe constraints on the spatial extension of the array.

In contrast, reactions with inverse kinematics (heavy ion beam on hydrogenated target) produce a naturally collimated neutron emission [21,22]. Using endothermal reaction enhances the focusing of the neutron emission in the forward direction. The neutron flux on the detector under study is thus increased, while the flux on the surrounding array is reduced. The neutrons are all produced within a small opening angle Θ_{max} given by

$$\sin^2\Theta_{max} = \frac{m_p M_f}{m_n M_i}\left(1 - \frac{E_{th}}{E_i}\right) \quad (3)$$

where E_{th} is the threshold energy, E_i is the incident kinetic energy, and M_i, m_p, m_n and M_f are the masses of the projectile, the proton, the neutron and the residual nucleus, respectively. In terms of the (negative) Q-value of the reaction, E_{th} is equal to $-Q(M_i + m_p)/m_p$. At a given angle relative to the beam axis $\Theta < \Theta_{max}$, there are two monoenergetic neutron groups with energies E_{n1} and E_{n2} given by

$$E_{n1,n2} = -\frac{2QM_i}{x(m_p + M_i)}\{x + \cos^2\Theta \pm \sqrt{\cos^2\Theta(x + \cos^2\Theta)}\} \quad (4)$$

where $x = E_{th}/E_i$, and terms of order Q/M_i and $(m_n - m_p)/M_i$ have been neglected.

The optimization of the neutron beam has been performed in experiments conducted at the tandem accelerator facilities of the Institut de Physique Nucléaire d'Orsay. Beams of ^{7}Li [21] and ^{11}B [22] have been tested using an oscillating hydrogenated polyethylene target with a thickness of 200 μg cm^{-2}. The beams were pulsed at 2.5 MHz with 5 ns wide bursts.

The contents of the induced neutron beams were studied by measuring the time-of-flight between the beam bursts and the arrival in an NE213 scintillation detector located at an angle of Θ varying from 0° to 25° at a distance of 110 cm away from the hydrogenated target. The time-of-flight spectra recorded at a ^{11}B beam energy of 35 MeV for different values of Θ are shown in Fig. 1. The two neutron groups (labeled n_1 and n_2) and the prompt γ produced in reactions in the hydrogenated target (labeled γ) are clearly seen. The positions of the n_1 and n_2 peaks follow the expectation of Eq. (4), as illustrated in Fig. 2, merging together when the maximum value

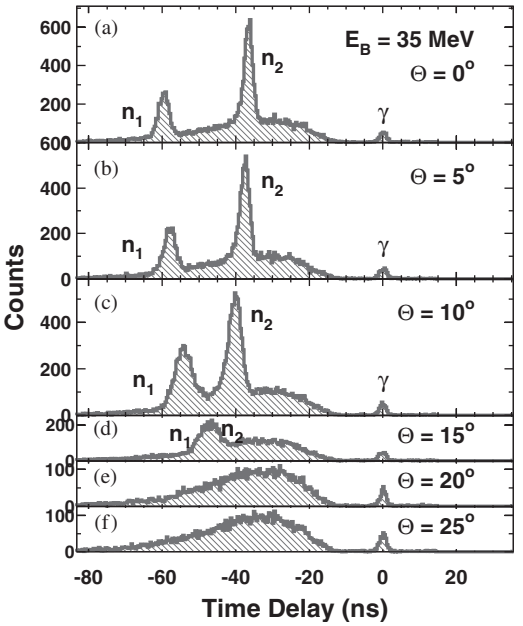

Fig. 1. Time-of-flight spectra between the arrival of the ^{11}B beam burst on the hydrogenated target and the detection of a particle in an NE213 neutron detector located at Θ angles varying from 0° to 25°. The incident ^{11}B beam energy is 35 MeV.

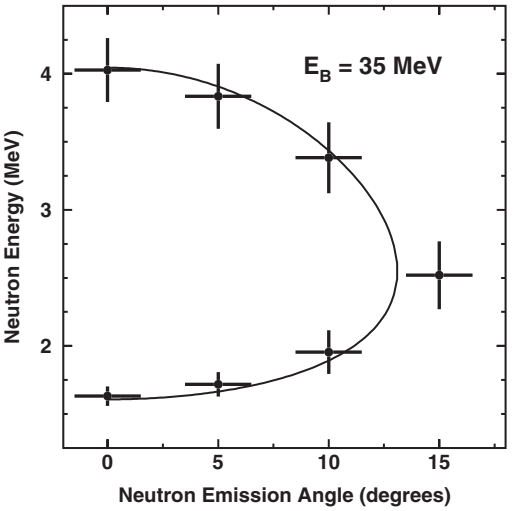

Fig. 2. Neutron energy as a function of the emission angle for the reaction p(^{11}B, ^{11}C)n at 35 MeV beam energy. The line is the expectation from Eq. (4). The experimental points correspond to the peaks observed in the preceding figure. The horizontal error bar corresponds to the solid angle of the neutron detector and the vertical one to the neutron energy spread associated to the width of the observed peaks.

$\Theta_{max} = 13.1°$ is reached. In addition, an important background under the n_1 and n_2 peaks is observed in Fig. 1. This continuum remains even beyond the Θ_{max} value imposed by the kinematics of the inverse (p,n) reaction. It is also present at all beam energies. It is therefore attributed to neutrons induced in fusion reactions on ^{12}C nuclei from the polyethylene target.

As shown in Fig. 3, this background is found to be less important with the ^{7}Li beams, which were therefore selected for the following experiments. The selected ^{7}Li beam energies for the NaI and Ge measurements are 13.7 and 14 MeV, corresponding to n_2 neutron kinetic energies at $\Theta = 0°$ of 2.15 and 2.32 MeV and maximum emission angles Θ_{max} of 11.5° and 13.4°, respectively.

The neutron beam energy resolution is dominated by the energy losses in the target (150 keV over the entire target thickness). The contributions from the Li beam properties themselves and straggling are 14 and 4 keV, respectively. The resulting uncertainty on E_n is 59 keV. The calculated neutron flux [21] is approximately of 10^5 n/s/str for a ^{7}Li beam intensity of 4 nA.

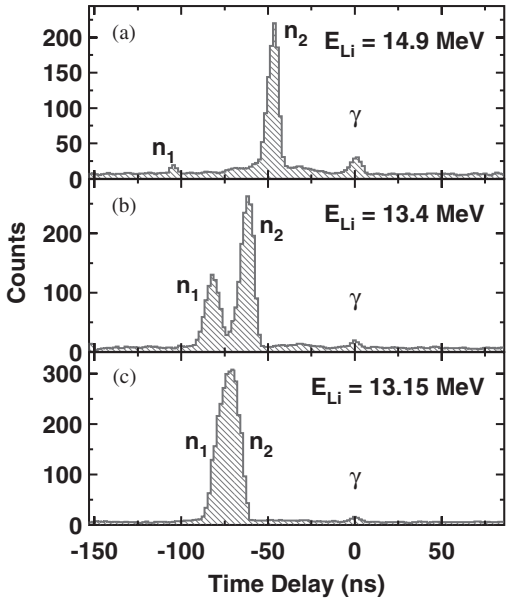

Fig. 3. Time-of-flight spectra between the arrival of the ^{7}Li beam burst on the hydrogenated target and the detection of a particle in the NE213 neutron detector at $\Theta = 0^\circ$ for ^{7}Li beam energies equal to (a) 13.15 MeV, (b) 13.4 MeV and (c) 14.9 MeV.

Table 1
Quenching values measured for Na recoils induced by the elastic scattering of 2.1 MeV neutrons for the different scattering angle values

θ (deg)	E_R(Na) (keV)	Q (%)
45	50±3	28.1±2.8
90	171±6	29.4±2.9
120	256±8	27.5±2.8
165	336±10	25.4±1.2

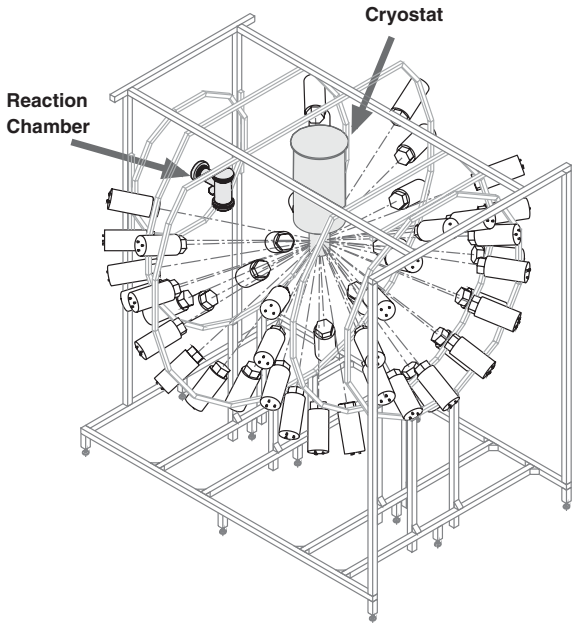

Fig. 4. Experimental setup with the four rings (45°, 90°, 120° and 165°) of neutron detectors and its support structure. The cryostat and the reaction chamber are also shown.

2.3. Neutron detector array

In the quenching measurements, the NE213 detector at $\Theta = 0^\circ$ is removed, and the detector under study is installed 60 cm away from the polyethylene target. The scattered neutrons are detected in an array of 48 NE213 scintillators located at a distance of 100 cm from the central detector and distributed in four rings corresponding to scattering angles of 45°, 90°, 120° and 165°. Thus, in one experiment the quenching factor is measured at four different values of θ, and consequently at four different values of E_R. The recoil energy values probed in the NaI and Ge experiments are listed in Tables 1 and 3.

The NE213 hexagonal cells have an external diameter of 10 cm and a thickness of 4 cm. A photomultiplier is optically coupled to each cell via a light guide. The support structure of the 48 neutron detectors is shown in Fig. 4. It is made of dural and steel, thin enough to minimize additional neutron scattering. The detector positioning is performed in the following way. First, a laser beam is propagated along the accelerator beam axis, simulating the neutron beam at $\theta = 0^\circ$. A rotating mirror is then set at the center of the array. The mirror is then tilted to the desired scattering angle and is rotated around the beam axis. The alignment of each NE213 detector is then adjusted so that the center of its front face is illuminated by the reflected laser beam.

2.4. Electronics

The background due to γ interactions in the NE213 cells is reduced by using the neutron–γ discrimination capabilities of these detectors. The signal coming from each detector is sent to two charge digitizers, integrating the current during $T_1 = 40$ ns and $T_2 = 400$ ns, respectively. The ratio of the corresponding integrated charges q_1 and q_2 provides a good γ/neutron discrimination.

The energy signal E_{ee} from the center detector is obtained with standard spectroscopy amplifiers in the cases of scintillation in NaI and ionization in Ge. The much slower heat signals of the Ge cryogenic detector are recorded with a wave form digitizer.

For each event, the following parameters are stored: the q_1 and q_2 values for all NE213 cells, as well as their time-of-flight relative to the beam burst, and the energy and time-of-flight measurements of the Ge or NaI(Tl) detector under study. As it will be seen, the time delay between the beam burst and the hit in the neutron detector is a powerful tool to identify true neutron scattering events. This delay Δt_{1-3} is the sum of those incurred as the neutron goes (i) from the polyethylene target to the center detector (Δt_{1-2}) and (ii) from that detector to an NE213 cell (Δt_{2-3}). With a fast center detector such as NaI, additional reduction of random coincidences may be achieved by a further discrimination on either Δt_{1-2} or Δt_{2-3}.

An event is defined as a coincidence between the center detector and at least one of the 48 neutron detectors. Data read-out is triggered by coincidences between any NE213 detector and the center detector within a time window of 1 μs. This width is chosen so as to accommodate the time resolution on the lowest energy signals in the center detectors.

The most delicate aspect of the trigger is to reconcile the speed of the NE213 signal read-out with the slowness of the coincidence decision. The solution adopted here is to initiate the digitization of the NE213 information as soon as any of them pass a certain threshold, and to hold this information until the coincidence decision with the slower Ge detector is issued. If no coincidence arrives, the NE213 electronics is reset. Otherwise, the NE213 data are further held until the end of the Ge heat and ionization read out, 250 ms later.

For the tests with the faster NaI detector, the width of the coincidence with the neutron array can be reduced to 500 ns, and the stand-alone NE213 pre-trigger is not necessary.

2.5. Recoil energy resolution

The accuracy of the determination of E_R on an event-by-event basis depends on the uncertainty on E_n and on θ. In natural Ge, an additional 2.6% r.m.s. fluctuation on E_R comes from the difference between the isotope masses.

The energy loss of the ^{7}Li ions in the hydrogenated target leads to a dependence of the neutron kinetic energy on the position of the reaction along the target length. For 2.32 MeV neutrons, the energy spread on E_n is $\pm 3\%$, leading to an equivalent spread on E_R. The main cause of event-by-event fluctuations of θ is the solid angle of the NE213 cells. Their contributions to the r.m.s. width of the E_R distribution decrease from 2.5 at 90° to 0.6% at 165°. All these effects taken together contribute to a 4% r.m.s. event-by-event fluctuation of E_R. This event-by-event uncertainty is much smaller than the resolution that can be achieved by a time-of-flight measurement over a distance of 1 m. It is also significantly smaller than typical resolutions for the measurement of E_{ee} in NaI(Tl) or Ge detectors.

3. Monte Carlo simulations

The experimental precision on Q arises from the possibility to select quasi-monoenergetic neutrons and from the simple kinematics of elastic collisions. The determination of E_R depends only on the kinematics of the neutron-producing reaction (yielding E_n) and the accurate positioning of the NE213 cells (yielding θ).

To preserve this simplicity, it is important to reduce as much as possible the multiple scattering of neutrons and all sources of beam-correlated signals between the target detector and the NE213 cells. To investigate this, the experiment for the

measurement of the heat and ionization quenching factors in Ge has been simulated using the Monte Carlo program GEANT [23]. In these simulations neutrons are produced one by one, thus assuming that the beam current and bunch structure is such that the pile-up of interactions coming from two different neutrons is negligible. In addition to the Ge detector, the simulation takes into account interactions occurring in the material composing 48 NE213 detectors and photomultipliers, the cryostat and the reaction chamber. It also takes into account the thickness of the hydrogenated target and follows the flight of the neutron from its creation to its detection in one of the NE213 cells. A cut on the time-of-flight similar to the one later applied to the data is also applied to the simulated data.

These simulations take into account the inefficiencies of the NE213 cells due to the experimental energy thresholds and their effect on the detection of the elastically and inelastically scattered neutrons (energies of 2.2 and 1.6 MeV, respectively: see below).

Predicted rates for elastic and inelastic scattering events, including multiple-scattering events, were derived from these simulations, assuming an integrated flux of 70 neutrons impinging on the Ge detector per second, corresponding to a ^{7}Li beam current of 5 nA. The single rate in the center Ge detector is approximately 10 neutrons per second.

Table 2 lists the Ge-NE213 coincident rates for the different event types described in the following.

Table 2
Simulated rates of Ge-NE213 coincidences after neutron identification and requiring that the neutron time-of-flight from the hydrogenated target to the NE213 counter is between 70 and 85 ns. The assumed incident yield on the target is 70 neutron/s

Process	Coincidence rate (/hour)		
	165°	120°	90°
Elastic	2.0	1.6	0.2
Inelastic	1.7	0.6	0.1
Multiple scattering inside Ge	1.0	0.6	0.1
Multiple scattering outside Ge	1.9	2.8	0.3

3.1. Inelastic neutron scattering

In addition to elastic scattering, neutrons can have inelastic interaction with Ge nuclei. The end products of such a collision are: (i) a nuclear recoil with a kinetic energy inferior to that associated with elastic scattering; (ii) a scattered neutron with a reduced energy and thus an increased time-of-flight to the NE213 cells; and (iii) a γ emission that may deposit some of its energy in the detector. Given the neutron energy, the most important γ's to be expected [24] are the 596 keV transition in ^{74}Ge, 835 keV in ^{72}Ge and 563 keV in ^{76}Ge. The simulation predicts that 82% of these γ escape detection, leaving only the neutron time-of-flight as a means to discriminate these events from elastic scatters. The cross-sections for each of these states are of the order of 1 b [24], compared with an elastic cross-section of the order of 2 b [25]. Given the isotopic abundances in Ge, the 563 keV yield is only a fifth of the 596 keV one.

The recoil energies produced by these inelastic processes are approximately 6 keV inferior to the values for elastic scattering. The differential cross-section of the inelastic process has a pronounced maximum for backward-scattered neutrons, and it is only at these angles that it can result in an appreciable background. At 120°, the coincident rate of inelastic events is approximately half of the elastic rate (Table 2). These two types of events can be identified by their $\sim$10 ns difference in arrival time in the NE213 cells, and thus can be treated separately.

In the 18% of cases where the γ is detected, most of the time it will leave only part of its energy via Compton scattering. The resulting distribution of energy deposited in the Ge will be flat, starting at the recoil energy and extending up to $\sim$500 keV.

3.2. Multiple interaction of a neutron in Ge

The interaction length of 2.32 MeV neutrons in Ge is approximately 6 cm. Despite the small size of the Ge detector chosen for the experiment (3.1 cm^3), incident neutrons have a 20% probability to interact twice or more in the crystal. The corresponding coincident rates are approximately half of the elastic rate (Table 2). It is not reduced

by the cut on the time-of-flight of the scattered neutron which is not significantly altered by the successive interactions. However, the angle of the outgoing neutron is uncorrelated with the energy deposited in the Ge detector. Some rejection of this background can be thus achieved, as single-scattering neutrons detected at a given angle θ should correspond to a single E_{ee} value within experimental resolution, while the corresponding distribution for multiple scatters is a continuum extending approximately from E_{ee} to twice E_{ee}.

3.3. Collisions in the surrounding materials

Neutrons can also have multiple interactions, with at least one occurring in the Ge and the other(s) in the materials surrounding the detector. In the SICANE setup, these additional interactions occur mainly in the cryostat[3] and the chamber containing the hydrogenated target. Once the time-of-flight requirements are applied, the coincidence rate of such events is predicted to be of the order of the elastic rate. However, for half of these events, the energy deposited in Ge is only a few keV and will not pass the trigger requirement. For the other half, the deposited energy is evenly distributed between 0 and E_{ee}.

In order to treat adequately the background of events coming from (i) inelastic recoils followed by Compton-scattering, (ii) multiple neutron scattering in the Ge itself, and (iii) multiple scattering in the surrounding material, a smooth background is included in the fits to the observed E_{ee} distributions yielding the average value at a given angle and time-of-flight selection.

4. Scintillation quenching factor of NaI(Tl)

As a first test of the performance of the SICANE facility, it was used for a measurement the scintillation quenching factor of NaI(Tl). Measurements with NaI(Tl) are considerably easier to perform than measurements with Ge. There is no need for a cryostat and in addition the good timing resolution provides an additional test

[3] The total thickness of the copper cryogenic shields is 4 mm.

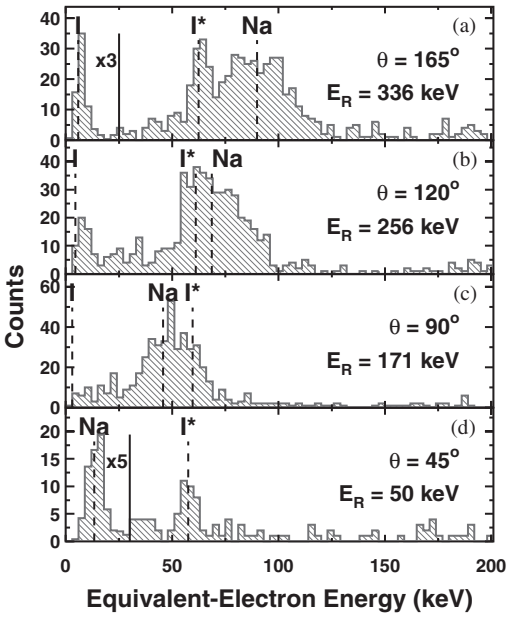

Fig. 5. Energy spectrum (in equivalent-electron keV) recorded in the NaI detector in coincidence with a neutron identified in an NE213 cell at $\theta = 165°$, 120°, 90° and 45° (a–d, respectively). The number of counts below 24 keV at 165° has been scaled down by a factor of 3 for clarity. The dashed lines show the expected peaks position for elastic (Na,I) and inelastic (I*) scatterings, assuming $Q(\mathrm{Na}) = 0.27$ and $Q(\mathrm{I}) = 0.09$.

to remove random coincidences: the neutron time-of-flight between the hydrogenated target and the NaI(Tl).

In order to reduce multiple scattering, the NaI(Tl) detector had a small size (25 mm diameter, 25 mm thickness). Its energy response E_{ee} for photons was calibrated in the energy range from 60 to 511 keV using ^{57}Co, ^{241}Am and ^{22}Na radioactive sources. With incident neutron energy of 2.1 MeV, only sodium recoils are observed at all four scattering angles of 45°, 90°, 120° and 165°.

To simulate the experimental conditions for the Ge experiment, the total count rate in the NaI(Tl) detector was limited to 35 Hz, yielding a coincidence count rate of 0.33 Hz. Fig. 5 shows recoil energy spectra recorded at different scattering angles after the selections on the neutron identification parameter in the NE213 cells and on the total neutron time-of-flight between the polyethylene target and the NE213. The largest peak observed in each spectrum corresponds to the

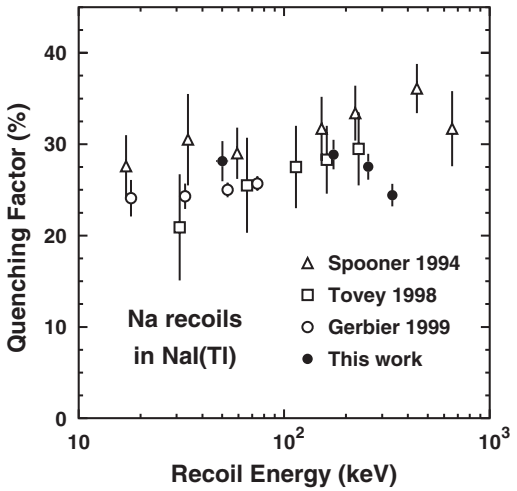

Fig. 6. Scintillation quenching factor for Na recoils in NaI(Tl) as a function of the recoil energy. The experimental data are from Refs. [6] and from this work.

elastic scattering of neutrons on Na nuclei. The peak around 60 keV, clearly seen at $\theta = 45°$, is due to inelastic scattering via the first excited state of ^{127}I. The structure below 10 keV evolving at the different angles could be due to neutron elastic scatterings on ^{127}I, producing a peak expected at approximately 6 keV at $\theta = 165°$, and at even lower energies at other angles. An additional cut on the time-of-flight between the NaI(Tl) and NE213 detectors does not remove a significant number of events. This indicates that the neutron identification and the total time-of-flight are sufficient to select a clean sample of neutron scattering events.

The E_R values for Na recoils in elastic scattering for the different scattering angle values and the corresponding quenching factors values are listed in Table 1. As shown in Fig. 6, the measured quenching factors are in good agreement with previous results [6]. Although the present measurement is based on a one-day test experiment, the statistical errors are already below the systematic uncertainties. At low recoil energy, the dominant uncertainty is the recoil energy due to the finite solid angle of the NE213 cells. At high recoil energy, the main uncertainty is the γ energy calibration.

5. Ionization and heat quenching factors of a germanium bolometer

5.1. Detector principle

The EDELWEISS collaboration [26] searches for WIMP Dark Matter using heat-and-ionization cryogenic germanium detectors, also called bolometers. The energy deposited in the detector produces two signals. First, the electron–hole pairs created by ionization are collected on electrodes implanted or vaporized on the surface of the crystal. Secondly, a thermistance measures the few microkelvin heating of the crystal due to (i) the thermalization of the electron or nuclear recoil from the primary interaction, and (ii) the Joule energy associated with the migration of the electron–holes due to the applied electric field. Whether the initial recoil is electronic or nuclear, the subsequent Joule heating (or Luke–Neganov effect [27]) depends only on the strength ionization signal, and thus is not affected by the quenching factor. Correcting for this effect in the presence of a bias V_o on the electrodes, the quenching factors associated with the ionization and recoil energy measurements (Q and Q', respectively) are

$$Q = \frac{E_I}{E_R} \tag{5}$$

$$Q' = \left(1 + \frac{V_o}{V_{pair}}\right)\frac{E_H}{E_R} - Q\frac{V_o}{V_{pair}} \tag{6}$$

where $V_{pair} = 2.96$ V is the electron–hole pair creation potential in Ge. E_I and E_H are, respectively, the electron-equivalent ionization and heat signal amplitudes, i.e. as calibrated used γ-ray sources. E_R is the recoil energy as given by Eq. (2).

5.2. Cryostat

For the measurement of its quenching factor, the cryogenic Ge detector is placed inside a dilution refrigerator. A base temperature of 25 mK was achieved; however, it was regulated at 35 mK in order to optimize the properties of the heat signal for this measurement. The thicknesses of the different screens of the cryostat were chosen to minimize neutron scattering. Special care was

taken to avoid mechanical vibrations. In order to isolate the cryostat from the beam line components and the multidetector array elements, it is maintained at beam height (1.8 m) with a wooden structure mounted on pneumatic insulators. A metallic platform above the cryostat facilitates liquid nitrogen and helium fills and access to the bolometer electronics. The center of the detector is 60 cm away from the polyethylene target.

5.3. Detector

The bolometer used in this work is a cylindrical crystal with a 10 mm height and a 20 mm diameter. In this prototype detector [28], the heat sensor is an NbSi thin film used as an Anderson insulator. The operating potential V_o is 6.26 V. To facilitate the detector monitoring, a weak collimated ^{57}Co source is mounted close to it.

Keeping the data rate as high as possible is desirable in this statistiċs-limited measurement. In this respect, an advantage of NbSi thin-film sensors relative to the NTD sensors normally used by the EDELWEISS collaboration (see e.g. Ref. [26]) is the relatively fast risetime and decay of the heat signal. These time characteristics depend on the temperature of the detector. At 35 mK, the risetime is approximately 1 ms and the decay of the signal has a fast ($\sim$4 ms) and a slow ($\sim$40 ms) components. The fast component is due to ballistic phonons and its amplitude depends not only on the deposited energy but also on the interaction point relative to the sensor. The slow component corresponds to thermal phonons and depends only on the deposited energy. It limits the acceptable interaction rate in the detector to approximately 15 Hz.

The electron-equivalent energy resolutions on ionization and heat signals in this experiment are 8 and 41 keV FWHM at 122 keV, respectively.

5.4. Ionization quenching factor of Ge

The ionization measurement has a trigger threshold of 17 keV. With a quenching value of approximately 30%, the expected ionization signal associated with neutron scattering in the 90° ring is only 18 keV. Consequently, the NE213 detectors were grouped on the 120° and 165° rings, corresponding to recoil energies of 93 and 123 keV, respectively.

Fig. 7 shows the time-of-flight spectra between the polyethylene target and the neutron detectors. In Fig. 7a, only those events rejected by the n/γ discrimination variable of the NE213 detectors are displayed. The peaks associated with photons produced either from γ or neutrons interacting in the Ge detector (labeled γγ and nγ, respectively) are clearly seen. Accepted events in the 120° and 165° rings are shown in Figs. 7b and c, respectively. The γγ and nγ peaks are strongly suppressed. Neutrons associated with an elastic interaction in the Ge detector are expected at time-of-flights of 77.1 and 77.4 ns, for the two respective rings. The broad structure from 20 to 40 ns corresponds to neutrons created in the polyethylene target hitting directly an NE213 cell without prior interactions. This implies that the energy deposit in the Ge detector is not related to the neutron in the NE213 cell, and could be

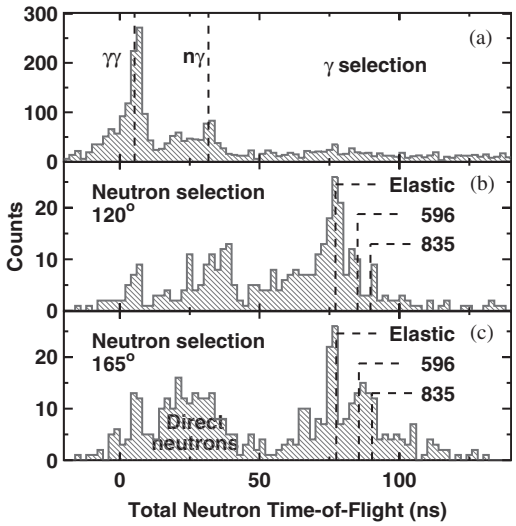

Fig. 7. Distribution of time-of-flights relative to the beam bursts, observed in the neutron detectors at 120° and 165° when selecting (a) events identified as γ, (b) events identified as neutrons at 120° and (c) at 165°. The time intervals expected for (γ,γ'), (n,γ), (n,n) or (n,n') scattering in the Ge detector are indicated as dashed lines. Direct neutrons are those going directly from the hydrogenated target to the neutron detector without passing through the Ge detector.

related to another particle emitted by another interaction in the polyethylene target in the same beam bunch.

The most important inelastic states expected to be excited are the 563 keV states in ^{76}Ge, 596 keV in ^{74}Ge, and 835 keV in ^{72}Ge. The corresponding time-of-flights are 84.5, 85.1 and 89.7 ns at 120°, respectively, and approximately 0.5 ns later at 165°. An excess of counts is indeed observed at these time-of-flights in Figs. 7b and c, especially at 165° where the simulations predict the largest inelastic yields.

To clearly assess whether these events are indeed due to inelastic scattering, the events are categorized according to three intervals of time-of-flight, corresponding to three scattering processes: 70 to 80 ns (elastic scattering), 80 to 87 ns (inelastic scattering with $E_\gamma = 563$ or 596 keV), and 87 to 92 ns (inelastic scattering with $E_\gamma = 835$ keV). The associated ionization spectra for these three categories at the two angles are shown in Fig. 8. A peak of events at low ionization energy is observed in each category. Its mean energy is largest in the elastic selection, and decreases with increased E_γ. The peak locations are consistent with those calculated (dashed lines) with the expected recoil energy for each event category, assuming a common quenching value of 33.3%. The fact that a flat background is more present in Figs. 8c–f than in Figs. 8a and b provides further support for the identification of inelastic scattering, as this behavior is expected as emitted photon may deposit some of its energy in the Ge detector. However, the relative amount of smooth background may also be partly due to the difference in the signal-to-background for each event category (as seen in Fig. 7).

A final check of the assignment of the events of Figs. 8c–f to inelastic collisions is to look back at the time-of-flight spectra of the neutron-selected events, but this time separating the events in two samples, according to the recorded ionization signal. Fig. 9a shows the time-of-flight spectra of events with ionization energies clearly associated with the peak observed in Figs. 8a and b, that is, between 25 and 50 keV at 120° and 40 and 65 keV at 165°. Fig. 9b shows the time-of-flight spectra of events outside this ionization energy intervals. As

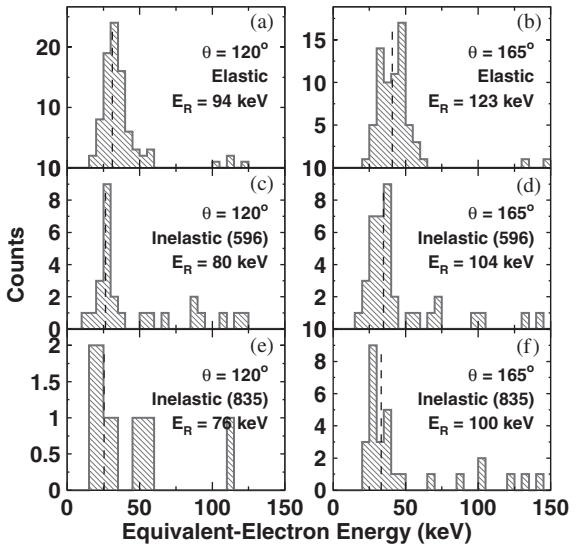

Fig. 8. Ionization energy spectra (in equivalent-electron keV) recorded in the Ge detector in coincidence with a neutron identified in an NE213 cell at $\theta = 120°$ (a,c,e at left) and 165° (b,d,f at right). The elastic selection (a and b) corresponds to total neutron time-of-flights of 70–80 ns, the "inelastic (596)" selection to 80–87 ns (c and d), and the "inelastic (835)" selection to 87–92 ns (e and f).

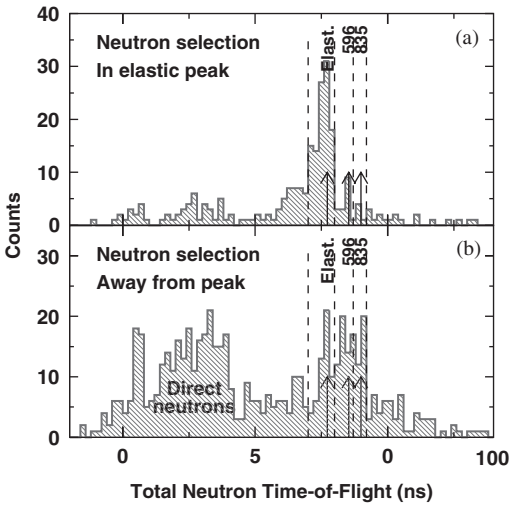

Fig. 9. Distribution of time-of-flights relative to the beam bursts, observed in the neutron detectors at 120° and 165° for events identified as neutrons, with (a) the cut on the ionization signal in Ge that favors elastic events (see text) and (b) the cut favoring inelastic events. The expected time-of-flights of elastic and inelastic events are marked with arrows. The dashed lines represent the three time-of-flight intervals used in the previous figure.

Table 3
Ionization quenching measured for Ge recoils induced by the elastic scattering of 2.32 MeV neutrons, for the different scattering angle values and scattering processes. The global systematic error on Q due to calibration and beam energy uncertainties is 3% (not included here)

θ	Process	E_R(Ge) (keV)	Q (%) (Stat. error only)
120°	Elastic	94±3	34.7±0.8
	Inel. (596)	80±2	32.8±0.9
	Inel. (835)	76±2	30.1±4.0
165°	Elastic	123±4	33.7±0.7
	Inel. (596)	104±3	31.4±1.2
	Inel. (835)	100±3	31.4±1.4
	Average		33.3±0.5

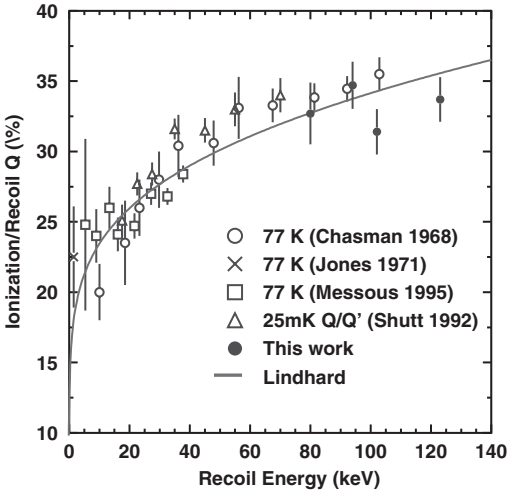

Fig. 10. Ionization quenching factor measured for Ge recoils in Ge(Li) detectors at liquid nitrogen temperature [11,12,14], and Ge recoils in hyperpure Ge at 35 mK (this work). The Q/Q' measurement of Ref. [13] is also displayed, assuming a heat quenching Q' of 100%. The thick line represents a calculation based on the Lindhard theory [16], as parametrized in Ref. [3].

expected, the elastic scattering peak is well suppressed in the second sample.

These tests clearly demonstrate the presence of inelastic scattering events, and indicate that the time-of-flight selection is adequate for identifying them, given the present statistics. This identification is important since the difference in recoil energy between elastic and inelastic scattering events is about 20%. An improper identification of the elastic sample leading to a contamination of inelastic events could have lead to a significant bias in the measurement of the quenching factor. In our case, assigning the elastic value for the recoil energy to all events in the 68–92 ns range would have reduced the average Q value measurement by 5%.

It should be noticed that, with sufficient statistics, inelastic events increase the number of recoil energies covered by the measurements, going down to lower values (see Fig. 8).

The quenching values extracted from Fig. 8 data are listed in Table 3 and shown in Fig. 10. The statistical precision on the average Q value obtained in a 1-day experiment is 2%. The results are consistent within statistical uncertainty with published results [11,13,14] and the Lindhard model calculations. No significant systematic shifts are observed between the measurements of Ge(Li) in liquid nitrogen or our measurement of hyperpure Ge at cryogenic temperatures, or between our direct measurement of Q and the Q/Q' measurement of Ref. [13] in the same temperature range.

5.5. Heat quenching factor of Ge

The analysis for the heat quenching follows closely that of the ionization channel. The neutron and time-of-flight selections are identical.

However, in addition to the significantly worse resolution of the heat signal relative to ionization, the slow components of the heat signals are strongly affected by pile-up and microphonics. In order to get a heat-to-ionization ratio of one for events clearly associated with photons (ionization above 100 keV and identification in the NE213 cell), it is necessary to impose that the energy deduced from the slow and fast components agree to within 75 keV. This ensures the integrity of the adjusted pulse shape, at the price of rejecting all surface events with anomalously large fast components. Clearly, the problem of pile-up is a strong limitation for quenching measurements with slow cryogenic detectors.

Given the reduced statistics, a meaningful measurement is only obtained for the total sample,

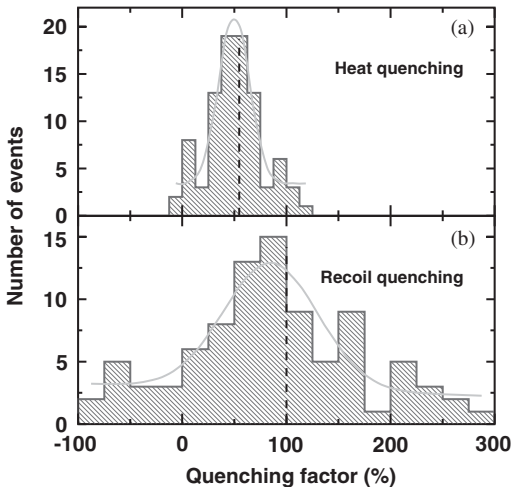

Fig. 11. Quenching factor for (a) the heat signal and (b) the recoil energy deduced from the difference between the heat and ionization signals. The full lines correspond to fits to the data yielding the values discussed in the text. The dashed lines represent the expected values assuming $Q = 33.3\%$ and $Q' = 100\%$.

dividing each measured energy by the recoil energy corresponding to the given angle and time-of-flight selection. The resolution does not allow for the identification of those inelastic events where the photon was partly detected. In order to be able to use inelastic events despite this problem, events with *ionization* quenching values below 20% and above 45% are rejected.

The resulting distribution of heat quenching values is shown in Fig. 11a. A Gaussian fit to the distribution gives an average quenching of $50 \pm 3\%$. Subtracting the Luke–Neganov effect corresponding to the applied electric field of 6.24 V using our measured average quenching value of 33.3%, we obtain (Fig. 11b) a quenching factor for the nuclear recoil part of the signal of $87 \pm 10\%$. The quoted error is statistical only; the systematic error, dominated by the large γ calibration uncertainties due to the poor resolution and limited statistics, is of the same order. Within these large errors, the result is consistent with the expected value, which should be very close to 100% [13,17].

This 1-day experiment clearly illustrates what can be achieved with this technique. The present statistical error would scale with the improvement of resolution in the heat channel. With sufficient energy resolution and statistics, a measurement at the percent level may be possible, if systematic effects such as inelastic scattering are kept under control.

6. Conclusion

The commissioning tests of the SICANE array and its setup confirm its high relevance for the calibration of the response of cryogenic detectors to nuclear recoils.

Using inverse reactions to produce a highly collimated neutron beam, no massive shielding of the neutron detectors is necessary, giving more freedom in their spatial setup. Competitive results have been obtained in a short running time (less than a day) for the quenching of scintillation in NaI(Tl) and of ionization in Ge. The array also makes possible a deeper investigation of the effect of inelastic scattering on the measurement.

The powerful diagnostic tools provided by the array (simultaneous measurements at different angles, neutron identification and time-of-flight measurements) are ideally suited for the study of cryogenic detectors. For such measurements, important factors that require proper attention are: (i) the slow response of the detector, and how it compares with the single rate in the cryogenic detector and the rate in coincidence with the neutron array; (ii) the rate in the neutron detector array due to neutron scattering in the material in the vicinity of the detector; and (iii) the ability to resolve inelastic and elastic events, either using the energy or using the time-of-flight measurements.

In addition, for the first time, it was directly verified that the ionization quenching factor of Ge at 35 mK is very close to that at liquid nitrogen temperature. This is consistent with the fact that the CDMS and EDELWEISS collaborations [13,19] obtain Q/Q' ratios compatible with the Q values measured at liquid nitrogen temperature [11,14] under the assumption that $Q' = 1$. Conversely, this last hypothesis is verified for the first time in the present work, albeit at a 15% level.

Acknowledgements

We thank the technical staff of the Tandem accelerator of Orsay, in particular D. Gardes, B. Waast and J.M. Curaudeau for their invaluable help. This work has been partially funded by the EEC-Network program under contract ERBFMRXCT980167.

References

[1] M.W. Goodman, E. Witten, Phys. Rev. D 31 (1985) 3059.
[2] M. Loidl, Proceedings of the XXXVIIth Rencontres de Moriond, Les Arcs, France, March 2002, astro-ph/0207308;
A. Morales, Nucl. Phys. Proc. 114 (Suppl.) (2003) 39;
L. Mosca, Nucl. Phys. Proc. 114 (Suppl.) (2003) 59.
[3] J.D. Lewin, P.F. Smith, Astropart. Phys. 6 (1996) 87.
[4] G. Jungman, M. Kamionkowski, K. Griest, Phys. Rep. 267 (1996) 195;
J. Ellis, A. Ferstl, K.A. Olive, Phys. Lett. B 481 (2001) 304.
[5] J. Graichen, et al., Nucl. Instr. and Meth. A 485 (2002) 774 and references therein.
[6] G. Gerbier, et al., Astropart. Phys. 11 (1999) 287;
D.R. Tovey, et al., Phys. Lett. B 433 (1998) 150;
N.J.C. Spooner, et al., Phys. Lett. B 321 (1994) 156.
[7] H. Park, et al., Nucl. Instr. and Meth. A 491 (2002) 460;
S. Pécourt, et al., Astropart. Phys. 11 (1999) 457.
[8] R. Hazama, et al., Nucl. Instr. and Meth. A 482 (2002) 297;
D.R. Tovey, et al., Phys. Lett. B 433 (1998) 150;
C. Bacci, et al., Astropart. Phys. 2 (1994) 117.
[9] D. Akimov, et al., Phys. Lett. B 524 (2002) 245.
[10] G. Gerbier, et al., Phys. Rev. D 42 (1990) 3211;
P. Zecher, et al., Phys. Rev. A 41 (1990) 4058.
[11] C. Chasman, et al., Phys. Rev. Lett. 21 (1968) 1430 and references therein.
[12] K.W. Jones, et al., Phys. Rev. C 4 (1971) 125.
[13] T. Shutt, et al., Phys. Rev. Lett. 69 (1992) 3425.
[14] Y. Messous, et al., Astropart. Phys. 3 (1995) 361.
[15] C. Amsler et al., Nucl. Instr. and Meth. A (2002) 494, and references therein.
[16] J. Lindhard, et al., Mat. Fys. Medd. Dan. Vid. Selsk. 33 (10) (1963) 1.
[17] A. Alessandrello, et al., Phys. Lett. B 408 (1997) 465;
A. Alessandrello, et al., Phys. Lett. B 384 (1996) 316.
[18] J.W. Zhou, et al., Nucl. Instr. and Meth. A 349 (1994) 225.
[19] A. Benoit, et al., Phys. Lett. B 479 (2000) 8.
[20] M.J.J van den Putte, et al., Nucl. Instr. and Meth. A 370 (1996) 271.
[21] A.H. Dave, et al., Nucl. Instr. and Meth. 200 (1982) 285.
[22] M. Drosg, Nucl. Instr. and Meth. A 254 (1987) 466.
[23] GEANT Detector Description and Simulation Tool, CERN Program Library, W5103, CERN, 1993.
[24] D. Lister, A.B. Smith, Phys. Rev. 183 (1969) 954.
[25] V. McLane, C.L. Dunford, P.F. Rose, Neutron Cross Sections, Vol. 2, Academic Press, New York, 1988.
[26] A. Benoit, et al., Phys. Lett. B 513 (2001) 8.
[27] M.P. Chapellier, et al., Physica B 284–288 (2000) 2135;
P.N. Luke, J. Appl. Phys. 64 (1988) 6858;
B. Neganov, V. Trofimov, USSR patent No. 1037771, 1981;
B. Neganov, V. Trofimov, Otkrytia i izobreteniya 146 (1985) 215.
[28] S. Marnieros, et al., Phys. Rev. Lett. 84 (2000) 2469;
A. Juillard, Ph.D. Thesis, Université de Paris-Sud, UFR Scientifique d'Orsay, France, October 25, 1999;
S. Marnieros, Ph.D. Thesis, Université de Paris-Sud, UFR Scientifique d'Orsay, France, May 18, 1998.